SAMPLE ORBIT COVARIANCE FUNCTION
and
FILTER-SMOOTHER CONSISTENCY TESTS

James R Wright,[*] **James Woodburn,**[†] **Son Truong,**[‡] **William Chuba**[§]

Abstract

We present two methods to validate our new *filter* orbit covariance function $Q_F(t_{k+1}, t_k)$. The first validation method derives from an ensemble of simulations to accumulate and propagate an orbit *sample* covariance function $Q_S(t_{k+1}, t_k)$ for comparison to $Q_F(t_{k+1}, t_k)$. *Sample* covariance $Q_S(t_{k+1}, t_k)$ is driven only by a potential function covariance matrix P. Consistency of $Q_F(t_{k+1}, t_k)$ with $Q_S(t_{k+1}, t_k)$ implies consistency of $Q_F(t_{k+1}, t_k)$ with P. The second validation method derives from processing real tracking data with our sequential filter-smoother to perform rigorous consistency tests. Test success validates $Q_F(t_{k+1}, t_k)$ and P, but test failure indicates filter modeling problems or an unrealistic potential function covariance matrix P.

INTRODUCTION

This is the second of three interrelated papers. The first paper[4], titled *Orbit Gravity Error Covariance*, is prerequisite to this paper, and the third paper[5], titled *Orbit Covariance Inner Integrals with Polynomials*, presents our new method to calculate and store the inner covariance integral. References to the first and third papers are given herein. All other references for this paper can be found in the first paper.

In the first part of this paper we describe techniques used in the validation of our new method to calculate the filter orbit error covariance function $Q_F(t_{k+1}, t_k)$ that is derived from gravity modeling errors. First, we present a new and independent orbit error *sample covariance function* $Q_S(t_{k+1}, t_k)$ to quantify effects of *approximations* in the orbit error *filter covariance function* $Q_F(t_{k+1}, t_k)$, identified in the first paper. The sample covariance function $Q_S(t_{k+1}, t_k)$ was constructed from an ensemble of one thousand numerical trajectory integrations from gravity acceleration variations that were derived from the covariance matrix P on potential function coefficient estimation errors. The sample covariance function $Q_S(t_{k+1}, t_k)$ is free of the approximations identified for $Q_F(t_{k+1}, t_k)$. The potential function covariance matrix P is represented with high fidelity in $Q_S(t_{k+1}, t_k)$. Thus the comparison of the sample orbit error covariance function $Q_S(t_{k+1}, t_k)$ to the filter orbit error covariance function $Q_F(t_{k+1}, t_k)$ quantifies the relation between $Q_F(t_{k+1}, t_k)$ and P.

In the second part of this paper we provide test results, from McReynolds' filter-smoother consistency test, due to processing real tracking data. These tests are effective in detecting significant modeling errors during the filter-smoother orbit estimation process.

SAMPLE COVARIANCE FUNCTION

Let C_{nm} and S_{nm} denote the coefficient values for degree n and order m of the potential function of interest, and let P denote the covariance matrix on estimation error random variables $\boldsymbol{\delta}\mathbf{C}_{nm}$ and

---

[*]ODTK Architect, Analytical Graphics, Inc., 220 Valley Creek Blvd, Exton, PA, 19341

[†]Chief Orbital Scientist, Analytical Graphics, Inc.

[‡]Systems Engineer, Analytical Graphics, Inc.

[§]Astrodynamics and Computer Science Senior Engineer, Analytical Graphics, Inc.

$\delta \mathbf{S}_{nm}$. A spectral (eigenspace) decomposition of P was performed and used to create 1000 sets of simulated coefficient estimation errors δC_{nm}^j and δS_{nm}^j , $j \in \{1, 2, \ldots, 1000\}$, from P and standard normal variates. Given initial orbit conditions for a low altitude orbit of interest, we performed 1001 numerical orbit propagations across a time interval $[t_0, t_F]$ where $t_F - t_0 = 2P$, and $P = $ orbit period. The first propagation created a simulated reference ephemeris due to use of gravity field for C_{nm} and S_{nm} with no other forces modeled. Using the same initial orbit conditions, we created 1000 perturbed ephemerides using $C_{nm} + \delta C_{nm}^j$ and $S_{nm} + \delta S_{nm}^j$, $j \in \{1, 2, \ldots, 1000\}$, with no other forces modeled. We differenced each of the 1000 simulated perturbed ephemerides with the simulated reference ephemeris to derive an ensemble of 1000 variations in position and velocity ephemerides to form a sample mean and sample covariance function $Q_S(t_{k+1}, t_k)$ about the mean.

POTENTIAL FUNCTIONS

Potential function covariance matrix cross-correlations are used (when available) in the calculation of the sample covariance function $Q_S(t_{k+1}, t_k)$, but they are not used in the calculation of the filter covariance function $Q_F(t_{k+1}, t_k)$. Only the diagonal variances are used in $Q_F(t_{k+1}, t_k)$.

EGM96 Geopotential

The EGM96 geopotential function coefficient covariance matrix is available as a full matrix. The EGM96 is complete through (deg,ord) = (70,70).

Covariance Matrix Cross-Correlations

There are 4 cross-correlations in the EGM96 geopotential coefficient errors whose magnitudes are greater than 0.95. For these cross-correlations, 1 of them is between longitude-dependent tesseral harmonic coefficients, and 3 of them are between global zonal harmonic coefficients. Three of these cross-correlations are negative. The positive cross-correlation is between zonals. These cross-correlations are used in the calculation of $Q_S(t_{k+1}, t_k)$.

Lunar-Prospector Potential

The Lunar-Prospector potential function coefficient covariance matrix is available as a full matrix, so cross-correlations are known. The Lunar-Prospector potential function version we have used is complete through (deg,ord) = (100,100).

Covariance Matrix Cross-Correlations

There are 102 cross-correlations between Lunar-Prospector potential coefficient errors whose magnitudes are greater than 0.95. For these cross-correlations, 99 of them are between longitude-dependent tesseral harmonic coefficients, and 3 of them are between global zonal harmonic coefficients. All cross-correlation values here are negative except for 2. Tesseral harmonic coefficients are longitude-dependent, and those not visible to the Earth are unobservable from range and Doppler measurements. So the negative cross-correlations are presumed to be explained by the absence of tracking data for the far-side of the Moon. These cross-correlations are used in the calculation of $Q_S(t_{k+1}, t_k)$.

GRACE Geopotential

We have used the GRACE geopotential function identified as GGM02C for all GRACE work reported on here. The GGM02C is complete in coefficient values through (deg,ord) = (90,90).

Covariance Matrix Cross-Correlations

The GRACE geopotential function coefficient covariance matrix is available only as a diagonal matrix, so cross-correlations are unknown. John Ries at University of Texas has been quoted as saying that GRACE cross-correlations are negligible.

ORBITS

JASON

At epoch 31 Aug 2003, $23^h 59^m 47.0^s$ UTC:

$$
\begin{bmatrix}
\text{semi-major axis} \\
\text{eccentricity} \\
\text{true argument of latitude} \\
\text{inclination} \\
\text{node} \\
\text{argument of perigee}
\end{bmatrix}
=
\begin{bmatrix}
a \\ e \\ u \\ i \\ \Omega \\ \omega
\end{bmatrix}
=
\begin{bmatrix}
1.21051 \text{ er} \\
0.000369594 \\
346.088 \text{ deg} \\
66.0654 \text{ deg} \\
145.850 \text{ deg} \\
332.458 \text{ deg}
\end{bmatrix}
$$

Dependent orbit element values:

$$
\begin{bmatrix}
\text{orbit period} \\
\text{true anomaly}
\end{bmatrix}
=
\begin{bmatrix}
P \\ v
\end{bmatrix}
=
\begin{bmatrix}
112.527 \text{ min} \\
13.6298 \text{ deg}
\end{bmatrix}
$$

JASON vs Typical-LEO Gravity Errors

The JASON semi-major axis $a_{\text{JASON}} = 1.2$ earth radii. The semi-major axis for a typical LEO is closer to $a_{\text{LEO}} = 1.1$ earth radii; e.g., $a_{\text{CHAMP}} = 1.07$ earth radii. Thus the JASON height is 0.1 er higher (637.8 km higher) than height for the typical LEO. Gravity acceleration degree-variances scale[1] with $\left[1/a^{2n+4}\right]$ for degree n. Table 1 quantifies[2] a comparison for gravity acceleration degree-variance scale between JASON semi-major axis and the semi-major axis for a typical LEO. Conclude that gravity acceleration errors for JASON are significantly less than for a typical LEO, and note that position errors are double integrals of acceleration errors with time.

Scale $\left[1/a^{2n+4}\right]$	$1/a^8$	$1/a^{12}$	$1/a^{20}$	$1/a^{36}$	$1/a^{68}$	$1/a^{132}$
Degree n	2	4	8	16	32	64
JASON $a = 1.2$ er	0.23	0.11	0.026	0.0014	4.1×10^{-6}	3.5×10^{-11}
typical $a = 1.1$ er	0.47	0.32	0.149	0.0323	1.5×10^{-3}	3.4×10^{-6}

Table 1: Degree-Variance Scale Factors

CHAMP

At epoch 20 May 2001, $00^h 00^m 00.0^s$ UTC:

$$
\begin{bmatrix}
\text{semi-major axis} \\
\text{eccentricity} \\
\text{true argument of latitude} \\
\text{inclination} \\
\text{node} \\
\text{argument of perigee}
\end{bmatrix}
=
\begin{bmatrix}
a \\ e \\ u \\ i \\ \Omega \\ \omega
\end{bmatrix}
=
\begin{bmatrix}
1.0675 \text{ er} \\
0.00405705 \\
38.2835 \text{ deg} \\
87.2768 \text{ deg} \\
34.6279 \text{ deg} \\
178.547 \text{ deg}
\end{bmatrix}
$$

---

[1] See the subsection *Kaula-Pechenick Gravity Auto-Correlation* of the first paper for the detailed presentation of this scale factor.

[2] Units are obtained on inspection.

Dependent orbit element values:

$$\left[\begin{array}{c} \text{orbit period} \\ \text{true anomaly} \end{array} \right] = \left[\begin{array}{c} P \\ v \end{array} \right] = \left[\begin{array}{c} 93.1864 \text{ min} \\ 219.737 \text{ deg} \end{array} \right]$$

LUNAR-PROSPECTOR

Values used for the lunar radius a_M and lunar gravitational constant μ_M:

$$\left[\begin{array}{c} a_M \\ \mu_M \end{array} \right] = \left[\begin{array}{c} 1738000.0 \text{ (m)} \\ 4902800238000.0 \text{ (m}^3/\text{s}^2) \end{array} \right] \tag{1}$$

Kepler Element Values

Initial orbit conditions in Kepler elements for Epoch 28 Feb 1999 0^H:0^M:0.0^S UTC:

$$\left[\begin{array}{c} a \\ e \\ u \\ i \\ \Omega \\ \omega \end{array} \right] = \left[\begin{array}{c} 1.017031 \text{ (LR)} \\ 0.000000 \\ 115.949 \text{ (deg)} \\ 89.4808 \text{ (deg)} \\ 195.078 \text{ (deg)} \\ 0.000000 \text{ (deg)} \end{array} \right] \tag{2}$$

Dependent orbit element values:

$$\left[\begin{array}{c} P \\ v \end{array} \right] = \left[\begin{array}{c} 111.1431 \text{ (min)} \\ 115.9491 \text{ (deg)} \end{array} \right] \tag{3}$$

The true argument of latitude u is well defined because $[0 < i < 180]$ (deg). But the true anomaly v and argument of perifocus ω are undefined for zero eccentricity. Set $\omega = 0.0$ arbitrarily for $e = 0.0$.

FILTER COVARIANCE VS SAMPLE COVARIANCE

The orbit gravity error process noise covariance function $Q_F(t_{k+1}, t_k)$ for the filter was compared with the sample covariance function $Q_S(t_{k+1}, t_k)$, in Gaussian-frame position coordinates, to establish the consistency, or lack thereof, of $Q_F(t_{k+1}, t_k)$ with $Q_S(t_{k+1}, t_k)$. This provides a method to establish the consistency, or lack thereof, of $Q_F(t_{k+1}, t_k)$ with P. All acceleration errors other than gravity modeling errors were ignored.

The filter process-noise covariance function $Q_F(t_{k+1}, t_k)$ was calculated according to the Kaula-Pechenick-Wright algorithm, driven by the covariance matrix P. This algorithm averages gravity acceleration perturbations over a sphere, thereby integrating out the effects of the local trajectory. Filter process-noise covariance calculations for $Q_F(t_{k+1}, t_k)$ are performed quickly, for use in real-time performance.

Sample error covariance calculations for $Q_S(t_{k+1}, t_k)$ are very time consuming. $Q_S(t_{k+1}, t_k)$ was calculated from 1000 separate ephemeris integrations, with gravity acceleration perturbations derived from a spectral decomposition of the full non-diagonal covariance matrix P. We assume here that the sample error RMS values represent the true orbit covariance, and we know that the filter process-noise 1-sigma values incur errors due to approximations invoked[4] for construction of the fast-running filter covariance $Q_F(t_{k+1}, t_k)$. Ideally we would prefer the filter process-noise 1-sigma values to be the same as, or slightly larger than, the sample error RMS values so as to minimize filter estimation errors and guarantee filter stability.

JASON-EGM96

JASON-EGM96 Figures 2, 3, and 4 present radial, intrack, and crosstrack position error curves for sample error root-mean-square (RMS) functions, overlaid with filter process-noise root-variance (1-sigma) functions.

The JASON-EGM96 sample covariance function $Q_S\left(t_{k+1}, t_k\right)^{EGM96}$ and the JASON-EGM96 filter covariance function $Q_F\left(t_{k+1}, t_k\right)^{EGM96}$ both use the full non-diagonal EGM96 covariance matrix P^{EGM96} values, but aside from this their calculations are independent and very different.

Inspection of Figures 2, 3, and 4 reveals that the sample variances are dominated by the filter variances in all three position components for the JASON two-orbit propagation times (225 minutes), except for the last 40 minutes of the intrack component. When not equal we prefer that the sample variances be dominated by the filter variances.

LUNAR-POSPECTOR

Lunar-Prospector (LP) results are presented in Figures 5, 6, and 7. We used the Lunar-Prospector gravitational potential function identified as LP100K in all work reported on here. For LP we show that our filter covariance function $Q_F\left(t_{k+1}, t_k\right)^{LP}$, derived from P^{LP} via Kaula theory, is not consistent across the propagation interval $[t_0, t_F]$ with our sample covariance function $Q_S\left(t_{k+1}, t_k\right)^{LP}$, derived from P^{LP} via numerical ephemeris propagation. Propagation of our sample orbit covariance function $Q_S\left(t_{k+1}, t_k\right)^{LP}$ reveals agreement between $Q_S\left(t_{k+1}, t_k\right)^{LP}$ and $Q_F\left(t_{k+1}, t_k\right)^{LP}$ for time t early in the propagation interval $[t_0, t_F]$, but as t is increased, the non-zero variance in the radial component of $Q_S\left(t_{k+1}, t_k\right)^{LP}$ approaches zero, while that of $Q_F\left(t_{k+1}, t_k\right)^{LP}$ increases. Covariance functions $Q_S\left(t_{k+1}, t_k\right)^{LP}$ and $Q_F\left(t_{k+1}, t_k\right)^{LP}$ diverge. The divergence may be explained by approximately one-hundred negative cross-correlations in the potential function covariance matrix P^{LP} whose magnitudes are greater than 0.95. A potential explanation derives from the fact that the moon is gravity gradient stabilized – does not rotate with respect to an Earth observer, so that estimated tesseral harmonic coefficients local to the far-side[3] of the moon are not directly observable.

To repeat, as t is increased, the non-zero variance in the radial component of $Q_S\left(t_{k+1}, t_k\right)^{LP}$ approaches zero. This behaviour of the sample orbit covariance function $Q_S\left(t_{k+1}, t_k\right)^{LP}$ makes a statement about P^{LP}: Covariance matrix P^{LP} is unrealistic.

JASON-GRACE

JASON-GRACE Figures 8, 9, and 10 present radial, intrack, and crosstrack position error curves for sample error root-mean-square (RMS) functions, overlaid with filter process-noise root-variance (1-sigma) functions. Most noticeable, both error curves have very small magnitudes in all three components.

The filter process-noise covariance function $Q_F\left(t_{k+1}, t_k\right)^{GRACE}$ is calculated according to the Kaula-Pechenick-Wright algorithm, driven by the diagonal GRACE covariance matrix P^{GRACE}. This algorithm averages gravity acceleration perturbations over a sphere, thereby integrating out the effects of the local trajectory. Filter process-noise covariance calculations for $Q_F\left(t_{k+1}, t_k\right)^{GRACE}$ are performed quickly, for use in real-time performance, whereas the sample error covariance calculations for $Q_S\left(t_{k+1}, t_k\right)^{GRACE}$ are calculated from 1000 separate ephemeris integrations, with gravity acceleration perturbations derived from the diagonal GRACE covariance matrix P^{GRACE}. Thus $Q_S\left(t_{k+1}, t_k\right)^{GRACE}$ provides a more accurate representation of P^{GRACE} than does $Q_F\left(t_{k+1}, t_k\right)^{GRACE}$.

Inspection of Figures 8, 9, and 10 reveals good visual agreement for 20 minute propagations in the radial component, and for 40 minute propagations in the intrack and crosstrack components. The filter variance dominates the sample variance in the radial component after 64 minute propagations (preferred), but the sample variances dominate the filter variances in the intrack and crosstrack components after 40 minutes (not preferred).

---

[3]The Japanese mission Selene may provide tracking data for the far-side of the moon to enable observability of associated tesseral harmonic coefficients.

Periodicity

Figure 1 presents a cartoon depicting edge-on the true orbit plane and the filter estimated orbit plane, intersecting at Earth center of mass. The crosstrack component of spacecraft estimation error can be defined by differencing position errors in three components, referred to an appropriate vector basis. Figure 1 suggests that crosstrack postion errors have two cycles per JASON orbit period (112.5 minutes) roughly. Figure 10 seems to agree with Figure 1 in periodicity for both the sample covariance and the filter covariance. As time evolves the acceleration errors integrate with lag into an accumulation of position errors. Thus the amplitudes of both periodic curves increase secularly with propagation time.

   Figures 8 and 9 present radial and intrack postion errors with one cycle per JASON orbit period, and secular increase with propagation time. Periodicity is initiated at the epoch for propagation time, with the small JASON orbit eccentricity (0.0037).

COMPARISONS BASED ON $\mathbf{Q}_S(t_{k+1}, t_k)$

Table 2 presents and compares spacecraft position maximum error RMS (1σ) values derived from propagation of $\mathbf{Q}_S(t_{k+1}, t_k)$ from 0.0 minutes to 112.5 minutes (one orbit period for JASON) with zero initial condition values. These values were derived from the sample covariance functions $\mathbf{Q}_S(t_{k+1}, t_k)$ presented above, and thus present sharp propagation bounds that depend directly on potential covariance matrices P^{GRACE}, P^{EGM96}, and P^{LP}. They do not include initial condition estimation errors, and they do not include effects due to acceleration modeling errors other than gravity.

max position error RMS	JASON-GRACE	JASON-EGM96	LUNAR-PROSP
Radial	0.26 cm	2.7 cm	7 m
Intrack	1.30 cm	14.0 cm	20 m
Crosstrack	0.33 cm	1.5 cm	2 m

Table 2: 220-Minute Propagation Position Error Bounds

COMPARISONS BASED ON $\mathbf{Q}_F(t_{k+1}, t_k)$

Here we present the results of a covariance analysis derived from use of the filter covariance function $Q_F(t_{k+1}, t_k)$. Simulated-true 11-day spacecraft trajectories were created for JASON and CHAMP, alternately using geopotential functions GRACE-GGM02C (deg,ord) = (90,90) and EGM96 (deg,ord) = (70,70) for acceleration modeling. This produced four truth ephemerides JASON-GRACE, CHAMP-GRACE, JASON-EGM96, and CHAMP-EGM96. Four sets of simulated GPS pseudo-range and carrier-phase measurements were generated from these four true trajectories for day one. Gravity error perturbed trajectories, and associated process noise covariance functions $Q_F(t_{k+1}, t_k)$ were then used to create four one-day filter runs. For each filter run the GPS measurements were processed by the ODTK sequential filter across the first day, and then the filter estimated orbit was propagated for ten days. The ten day propagation was used to magnify propagation error covariance. Maximum 2σ values were derived from variances (σ^2) for each ten day covariance propagation. The simulated and estimated trajectories were differenced and graphed with $\pm 2\sigma$ filter covariance boundaries overlaid. Each of the three RIC position error component root-variance boundaries for each of the four filter runs, across the ten day propagation, are monotonically increasing, each with maximum values at the end of the ten day propagation. Maximum 2σ value position errors at the ten day propagation time are presented in Table 3.

   The use of the sample covariance function $Q_S(t_{k+1}, t_k)$ for accuracy analysis provides sharp lower bounds for propagation, but these bounds do not reflect the existence of estimation errors. Our use

of sample size requiring 1000 numerical ephemeris integration runs prohibits exhaustive sampling of the analysis parameter space.

The use of the filter covariance function $Q_F(t_{k+1}, t_k)$ for accuracy analysis generates pessimistic results, but these results represent an infinite sample size, are obtained quickly, and they provide the combined effects of propagation errors and estimation errors.

$(\mathbf{max}\ \mathbf{2\sigma})_{\mathbf{10d}}$ **(m)**	**Radial**	**Intrack**	**Crosstrack**
JASON-GRACE	0.07	7.50	0.08
CHAMP-GRACE	0.28	35.00	0.34
JASON-EGM96	1.10	120.00	1.28
CHAMP-EGM96	9.50	1200.00	10.50

Table 3: 10-Day Propagation Position Error Bounds

JASON vs CHAMP

Use Table 3 to compare **JASON-GRACE** to **CHAMP-GRACE**, and to compare **JASON-EGM96** to **CHAMP-EGM96**, to see the effect of spacecraft height on position accuracy improvement of JASON relative to CHAMP at the ten-day propagation time. JASON is 0.1 earth-radii higher (637.8 km higher) than CHAMP, so JASON position errors are much smaller than those of CHAMP from gravity acceleration modeling errors at all propagation times. See Table 1 for an explanation of height dependence in terms of gravity acceleration modeling errors.

GRACE vs EGM96

Use Table 3 to compare **JASON-GRACE** to **JASON-EGM96**, and to compare **CHAMP-GRACE** to **CHAMP-EGM96**, to see the apparent accuracy improvement of GRACE relative to EGM96 for a ten-day propagation following optimal filtering for one day.

PESSIMISTIC $\mathbf{Q}_F(t_{k+1}, t_k)$ PROPAGATION

Figures 11, 12, and 13 present position errors in radial, intrack, and crosstrack components for the CHAMP spacecraft using the EGM96 geopotential function and geopotential covariance matrix with simulated GPS data. Acceleration perturbations are derived from a spectral decomposition of the EGM96 geopotential covariance matrix. Filtering of simulated GPS data is performed for the first day (1440 minutes). Following this a ten-day (14400 minutes) propagation is performed using the last filtered estimate as initial conditions. The x-axis for each figure thus spans 15840 minutes. The y-axis unit is *meters*. The interior red line on each graph presents the difference between the simulated true spacecraft positions and filtered and propagated positions. The exterior black envelope presents $\pm 2\sigma$ boundaries derived from the filter covariance function $Q_F(t_{k+1}, t_k)$.

The estimation errors in red appear to be consistent with the covariance $\pm 2\sigma$ boundaries in black during the one-day filter processing interval. But the most noticeable graphical feature here is the contrast in magnitude between estimation error *propagations* in red and covariance *propagations* in black: The propagated error variances are large as compared to the propagated estimation errors. Several hypotheses have been advanced to explain this apparent dichotomy.

Filter Aliasing

On inspection, the semi-major axis (energy parameter) estimate presented in Fig. 14 appears to be negatively biased, particularly near the end of the one-day filter interval. Absorption of geopotential estimation error into the orbit semi-major axis estimate would be an aliasing of geopotential error

into orbit error. Could it be that potential energy estimation error is aliased from EGM96 into the orbit semi-major axis estimate? Might this explain the small propagated errors (red) in radial and intrack position components?

Cross-Correlations in P

Lunar-Prospector (LP) results presented in Figures 5, 6, and 7 may explain the effect of significant negative cross-correlations in P on the divergence between estimation error *propagations* in red and covariance *propagations* in black.

Constant I1 Integral Scalars

Covariance Approximation 7, presented in the first paper[4], is responsible for inflating $Q_F\left(t_{k+1}, t_k\right)$ filter values as compared to $Q_S\left(t_{k+1}, t_k\right)$ truth values.

FILTER-SMOOTHER CONSISTENCY TESTS

The filter-smoother consistency test theorem was derived by McReynolds[1][2][3] in 1980. The filter and smoother state estimate errors are assumed to be multi-dimensional Normal. Each component of the state estimate error is serially correlated, but is considered separately[4] here of other components.

Calculate the $N \times N$ difference matrix $\bar{P}_{k|L}$ between the filtered covariance matrix $\hat{P}_{k|k}$ and the smoothed covariance matrix $\tilde{P}_{k|L}$ for time t_k:

$$\bar{P}_{k|L} = \hat{P}_{k|k} - \tilde{P}_{k|L} \tag{4}$$

for each $k \in \{0, 1, 2, \ldots, L\}$. The difference matrix $\bar{P}_{k|L}$ should have no negative eigenvalues. Denote the square root of the ith main diagonal element of the $N \times N$ difference matrix $\bar{P}_{k|L}$ as $\sigma^i_{k|L}$. Also calculate the $N \times 1$ difference matrix $\bar{X}_{k|L}$ between filtered state estimate $\hat{X}_{k|k}$ and smoothed state estimate $\tilde{X}_{k|L}$ for time t_k:

$$\bar{X}_{k|L} = \hat{X}_{k|k} - \tilde{X}_{k|L} \tag{5}$$

Denote the ith element of the $N \times 1$ difference matrix $\bar{X}_{k|L}$ as $\bar{X}^i_{k|L}$. Now calculate and graph the ratio :

$$R^i_{k|L} = \bar{X}^i_{k|L} / \sigma^i_{k|L} \tag{6}$$

for each $i \in \{1, 2, \ldots, N\}$ and for each $k \in \{0, 1, 2, \ldots, L\}$.

Test

If for each $i \in \{1, 2, \ldots, N\}$ and for each $k \in \{0, 1, 2, \ldots, L\}$ we have:

$$\left|R^i_{k|L}\right| \leq 3 \tag{7}$$

with probability 0.99, then McReynolds' filter-smoother test is satisfied for all state components. If for each $i \in \{1, 2, \ldots, N\}$ and for each $k \in \{0, 1, 2, \ldots, L\}$ we have:

$$\left|R^i_{k|L}\right| > 3 \tag{8}$$

then McReynolds' filter-smoother test is failed for all state components. For each i for which inequality 7 is satisfied McReynolds' filter-smoother test is satisfied for that state estimate element, and for each i for which inequality 8 holds McReynolds' filter-smoother test is failed for that state estimate element.

---

[4] When all state estimate error components are considered jointly and simultaneously, coupled state estimate error component test acceptance thresholds would be required. Since large error cross-correlation magnitudes are observed, this could provide a useful state component coupled filter-smoother consistency test.

Results

Figs. 17, 15, and 16 present our filter-smoother consistency test results due to processing real tracking data. The JASON-EGM96 filter-smoother consistency test passes in all position components. The LUNAR-PROSPECTOR filter-smoother consistency test passes in all position components.

The JASON-GRACE filter-smoother consistency test fails in the crosstrack position component, but passes in the radial and intrack components. The filter-smoother consistency test is very sensitive to any and all modeling errors. Modeling error candidates include (but are not limited to) an inadequate solar pressure model for JASON, lack of a thermal venting model for JASON, and an optimistic GRACE geopotential function covariance matrix. Fig. 18 presents our JASON filter-smoother estimate (blue) and 2σ bounds (black) for solar pressure correction after processing real GPS pseudo-range and carrier-phase tracking data. We modeled $C_P = 0.42$ for the filter input, but the corrections are periodic with the JASON orbit period and have amplitude equal to $C_P = 0.42$. The spherical body model with two-cone shadowing for solar pressure is clearly inadequate, and explains, in part, the filter-smoother consistency test failure.

References

[1] Stephen McReynolds, *Private Communications*, 1980 to 1998.

[2] Stephen McReynolds, *Editing Data Using Sequential Smoothing Techniques for Discrete Systems*, AIAA/AAS Astrodynamics Conference, August 20-22, 1984, Seattle, WA.

[3] Stephen McReynolds, *Filter-Smoother Consistency Test*, Interoffice Memo, Martin Marietta, 21 Feb., 1995

[4] Wright, James R., Woodburn, James, Truong, Son, Chuba, William, *Orbit Gravity Error Covariance,* 18th AAS/AIAA Space Flight Mechanics Meeting, Paper AAS 08-157, Galveston, TX, January 2008

[5] Wright, James R., Woodburn, James, Truong, Son, Chuba, William, *Orbit Covariance Inner Integrals with Polynomials*, 18th AAS/AIAA Space Flight Mechanics Meeting, Paper AAS 08-161, Galveston, TX, January 2008

Crosstrack Position Error

(two cycles per orbit period)
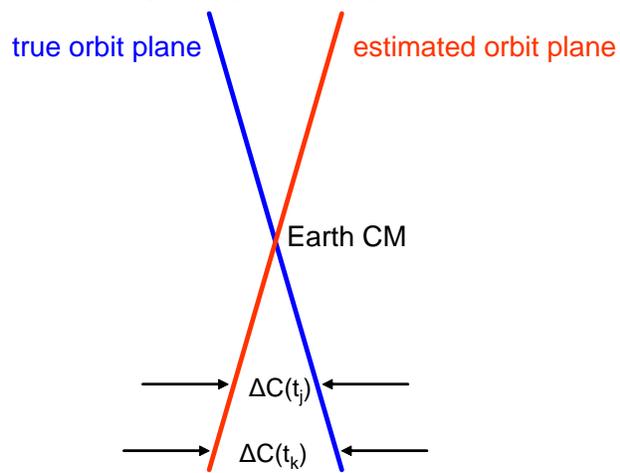
Figure 1: Periodic Crosstrack Position Error Cartoon

JASON and EGM96

EGM96 Commission (deg,ord) = (70,70), No Omission
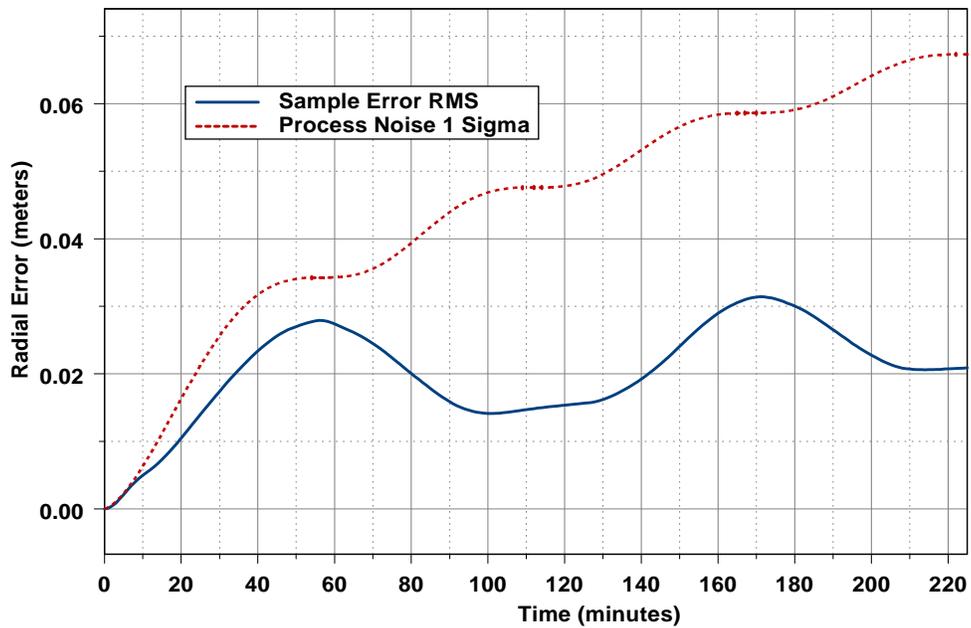
Figure 2: JASON-EGM96 Radial Position Error
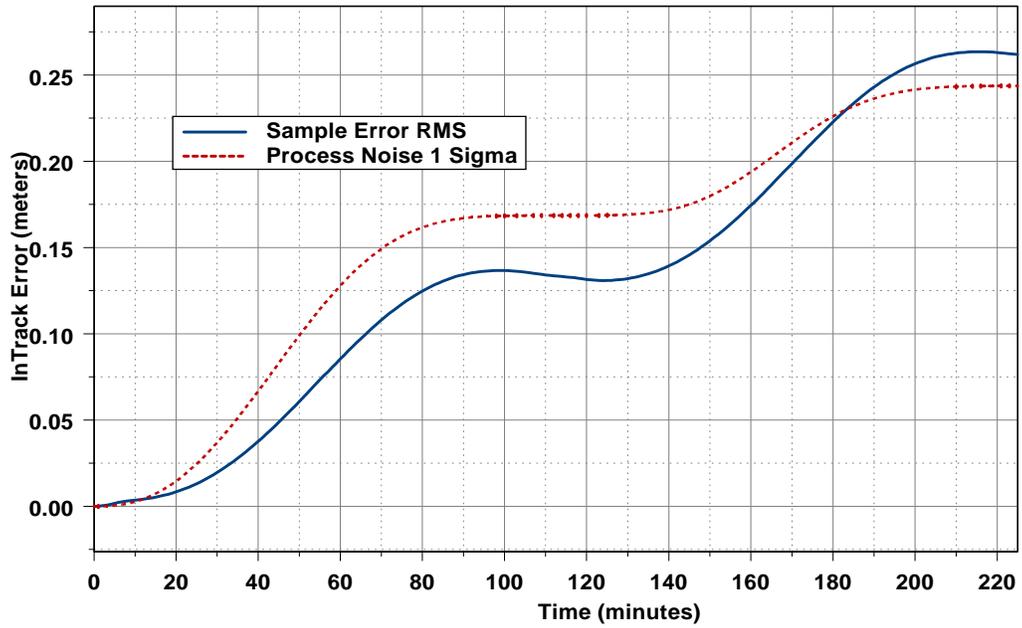
Figure 3: JASON-EGM96 Intrack Position Error
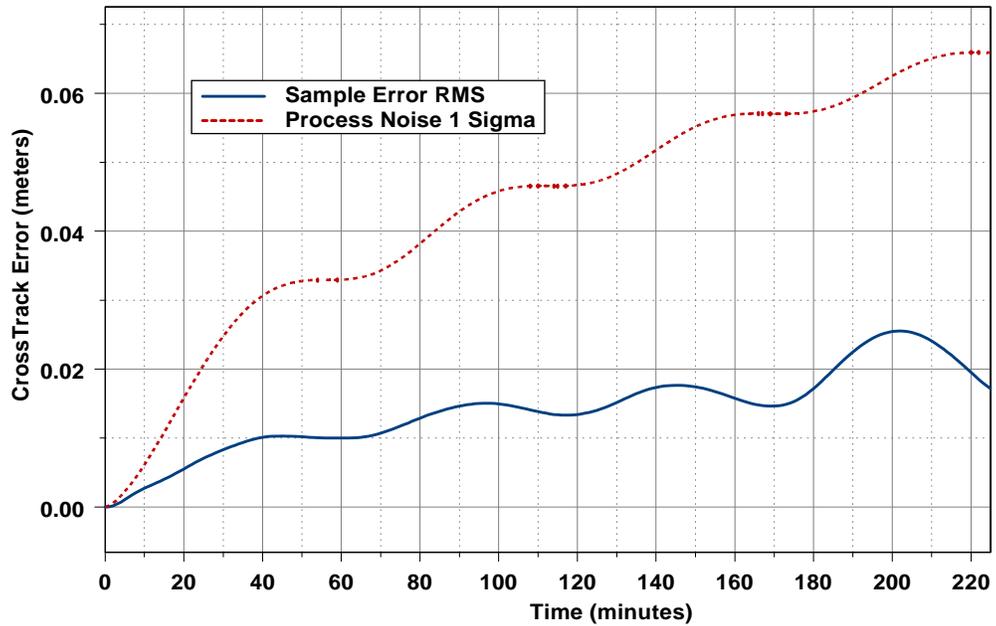
Figure 4: JASON-EGM96 Crosstrack Position Error

LP100K 100x100, 1000 Samples
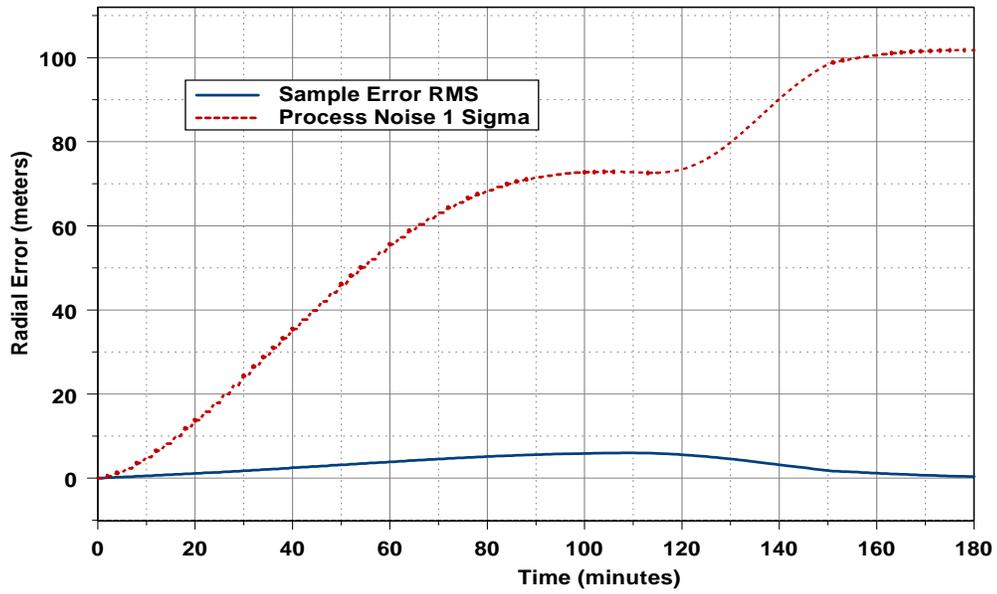
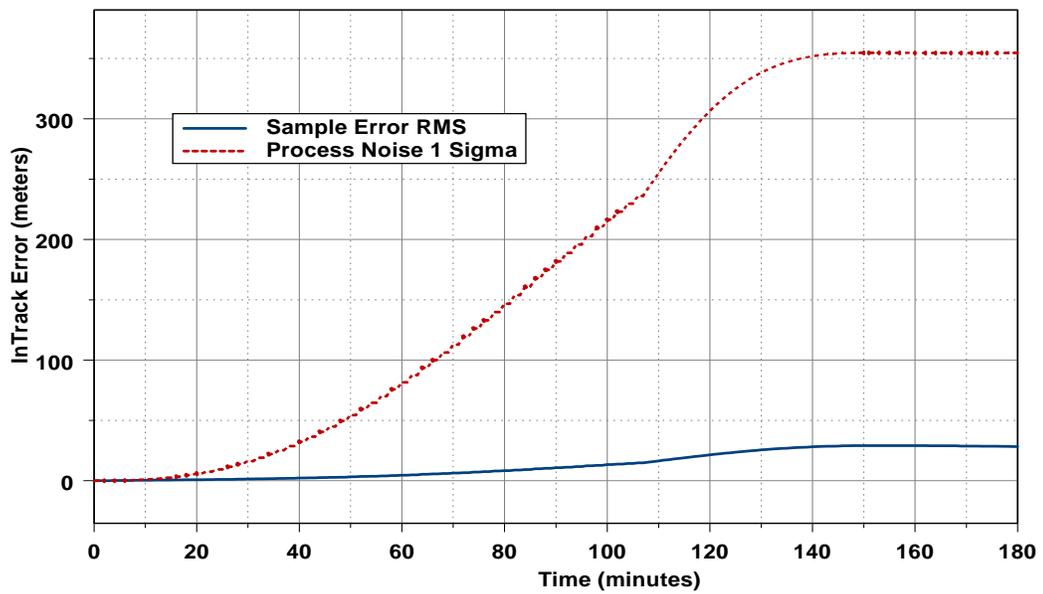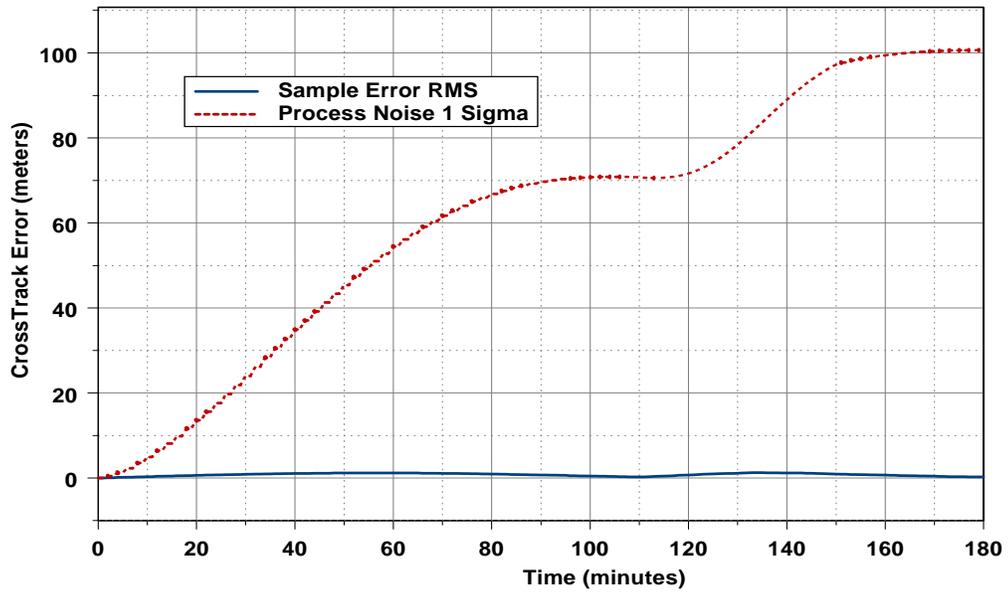Figure 5: Lunar-Prospector Radial Position Error

LP100K 100x100, 1000 Samples

Figure 6: Lunar-Prospector Intrack Position Error

Figure 7: Lunar-Prospector Crosstrack Position Error

Figure 8: JASON-GRACE Radial Position Error

JASON and GRACE

GGM02C Commission (deg,ord) = (90,90), No Omission
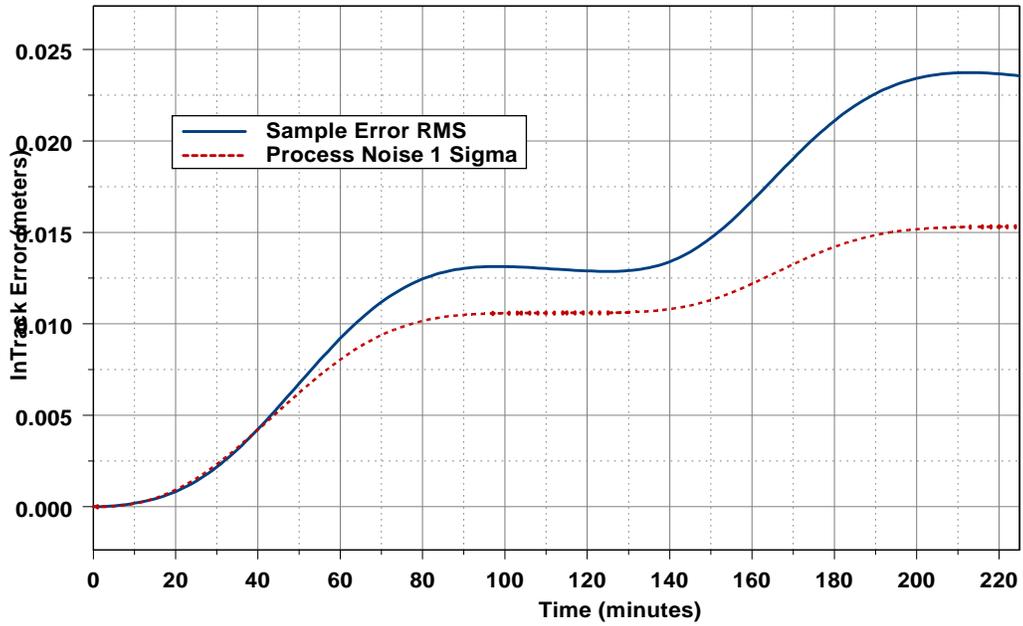
Figure 9: JASON-GRACE Intrack Position Error

JASON and GRACE

GGM02C Commission (deg,ord) = (90,90), No Omission
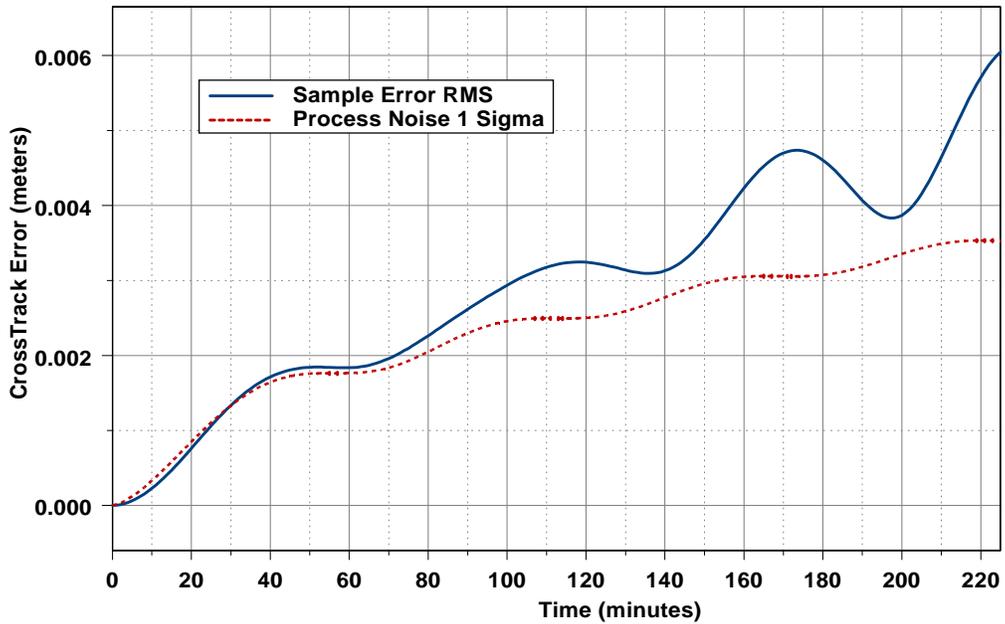
Figure 10: JASON-GRACE Crosstrack Position Error
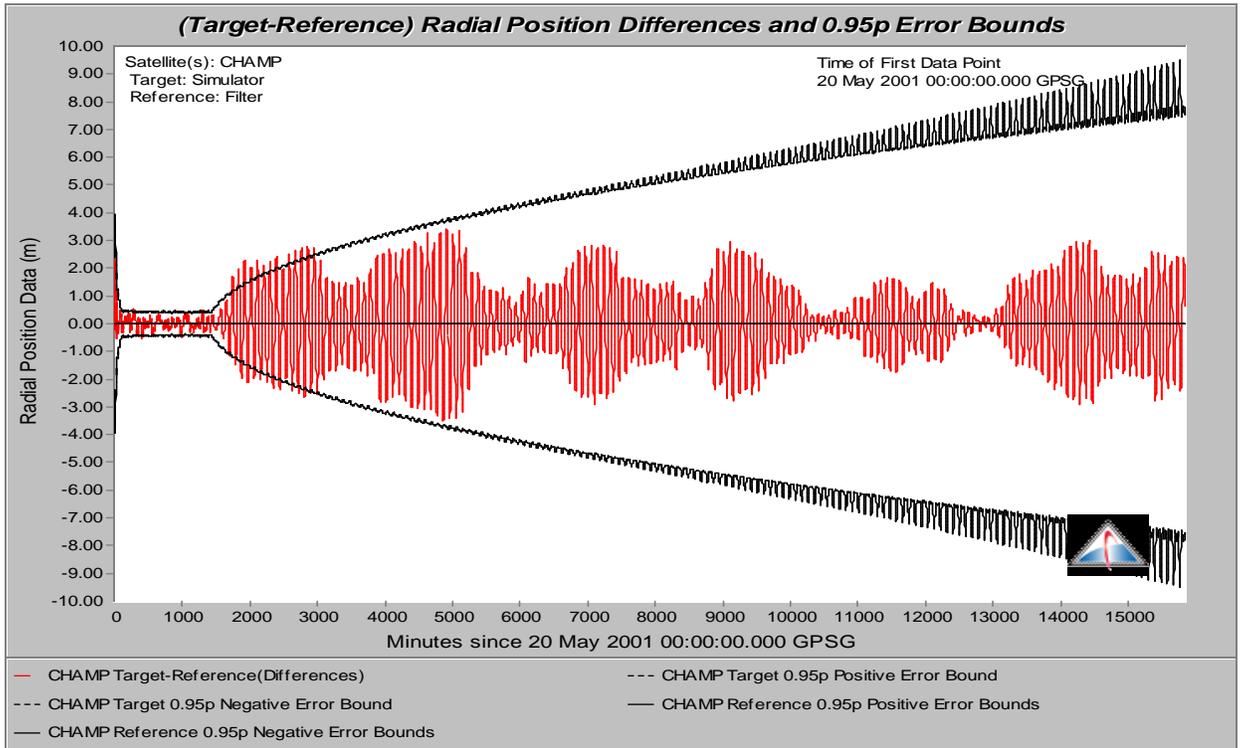
Figure 11: Radial Position Errors CHAMP-EGM96
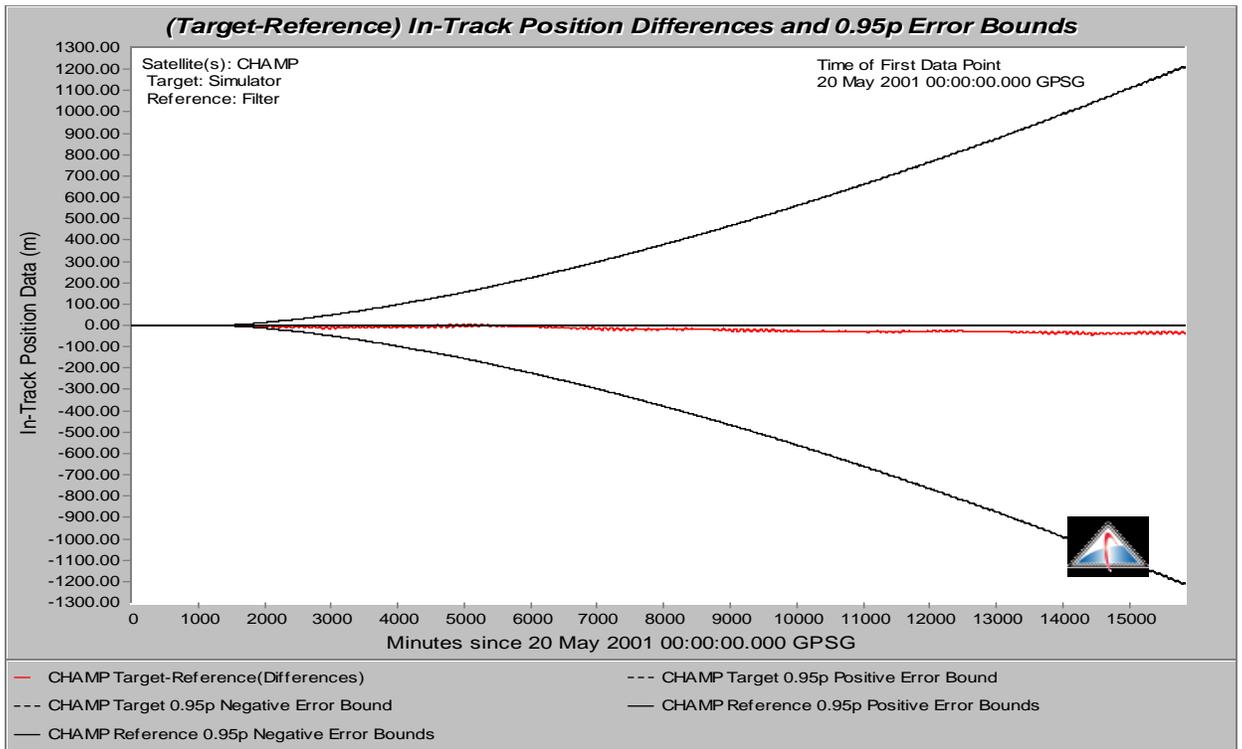
Figure 12: Intrack Position Errors CHAMP-EGM96
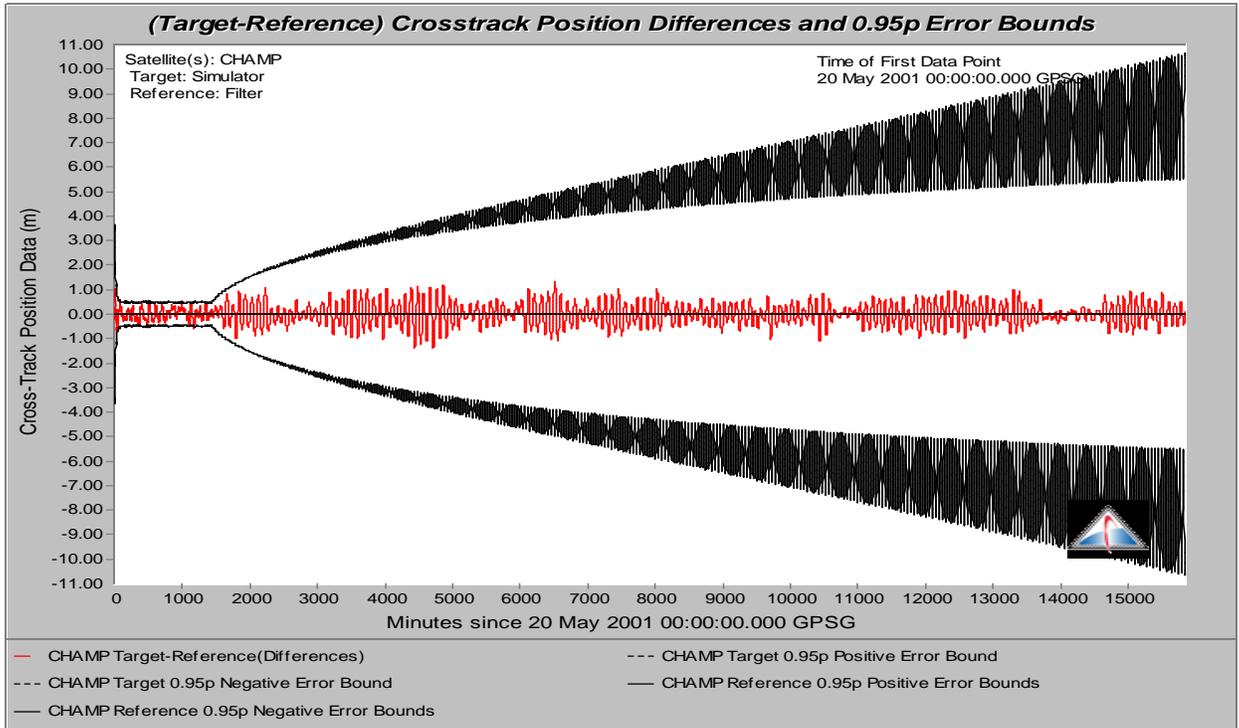
Figure 13: Crosstrack Position Errors CHAMP-EGM96
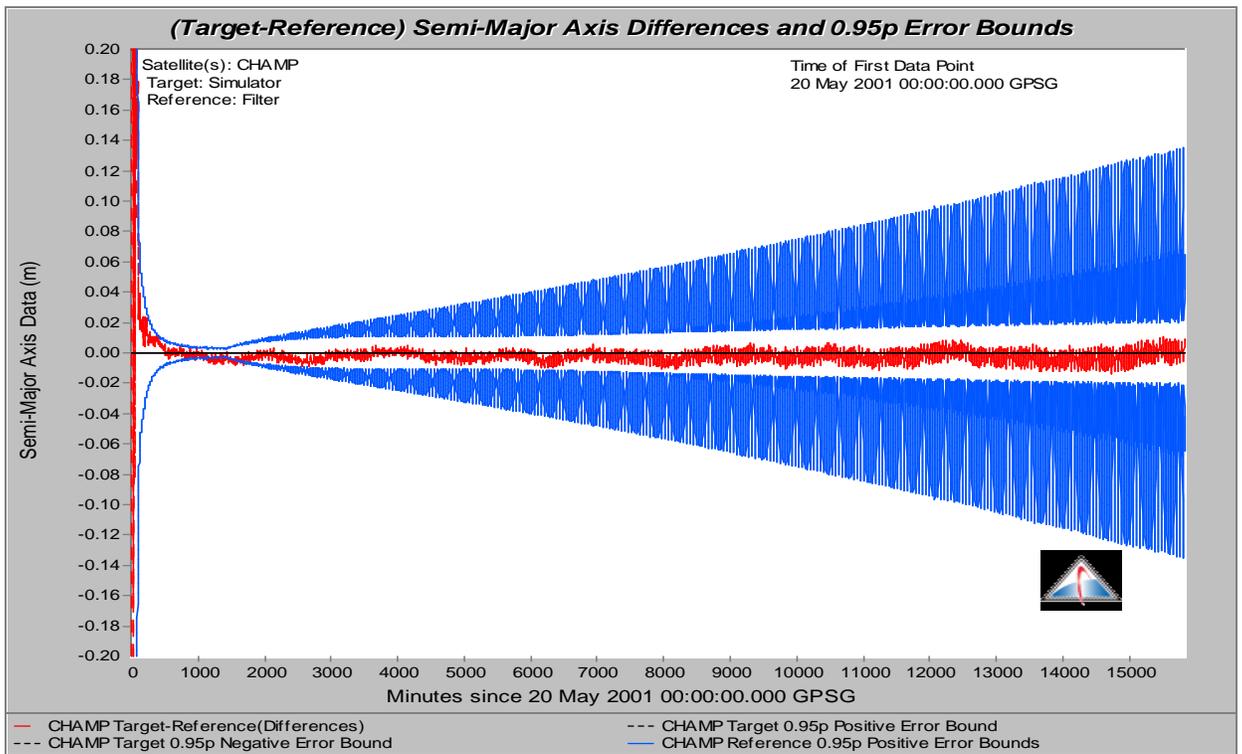
Figure 14: Semi-major Axis Filter Errors
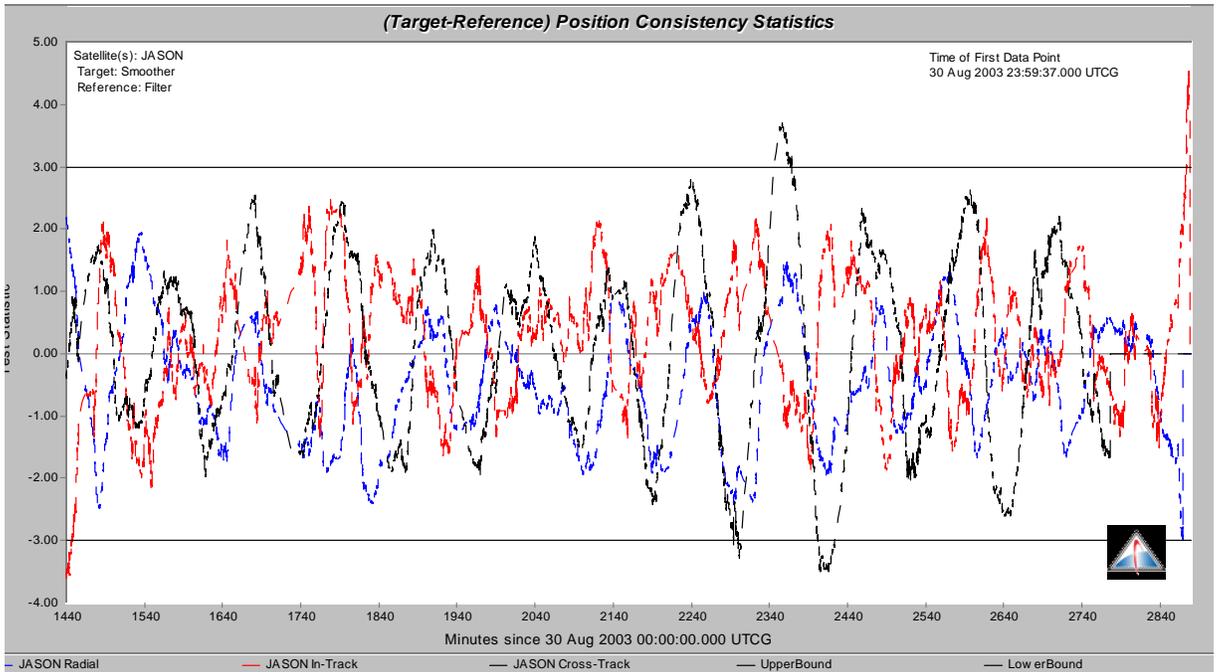
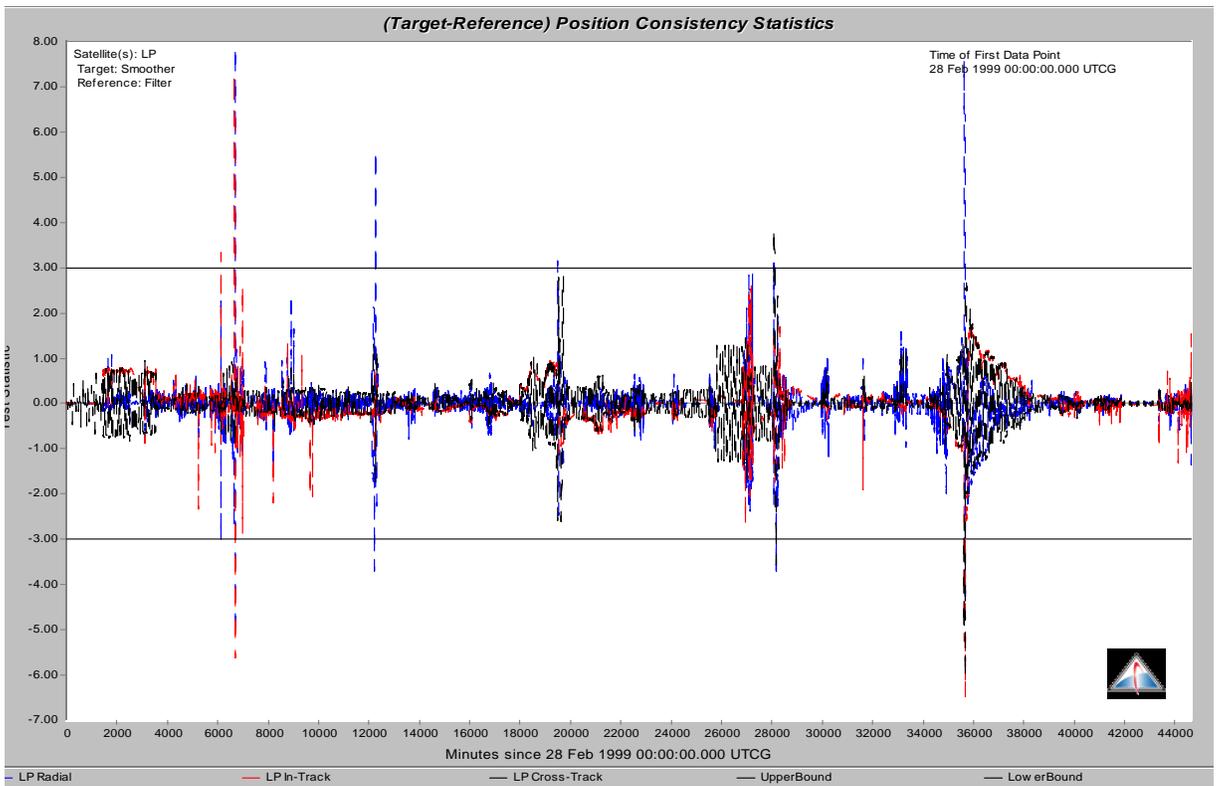Figure 15: JASON-EGM96 Filter-Smoother Consistency Test 3

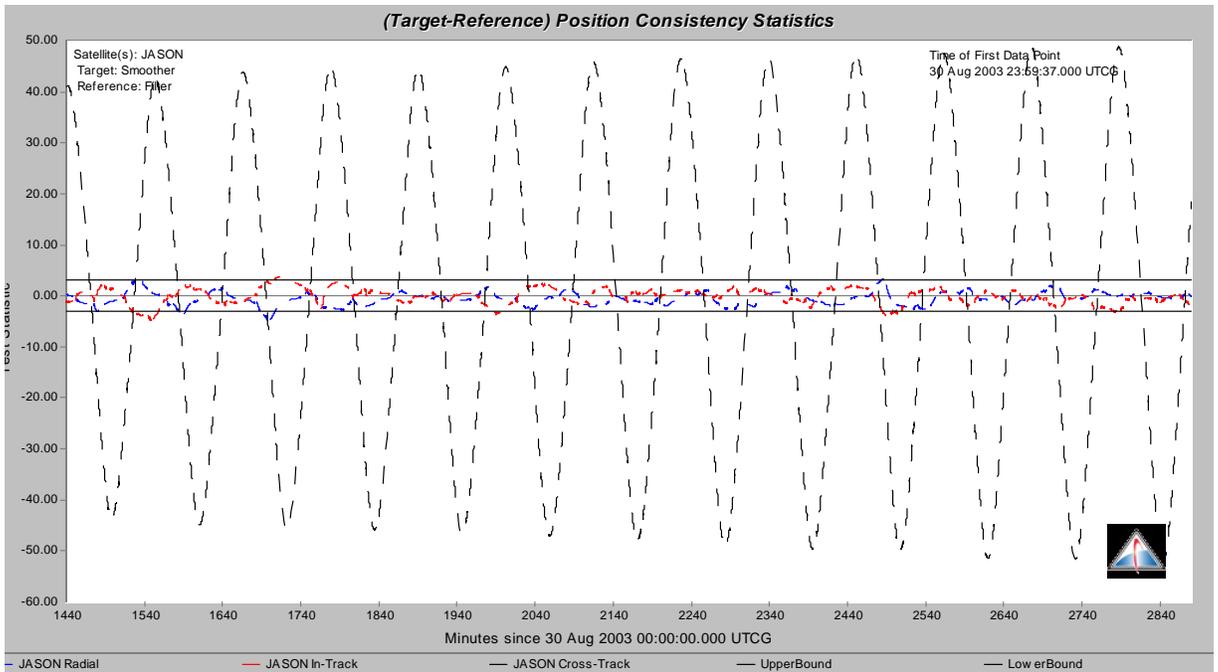Figure 16: LUNAR-PROSPECTOR Filter-Smoother Consistency Test

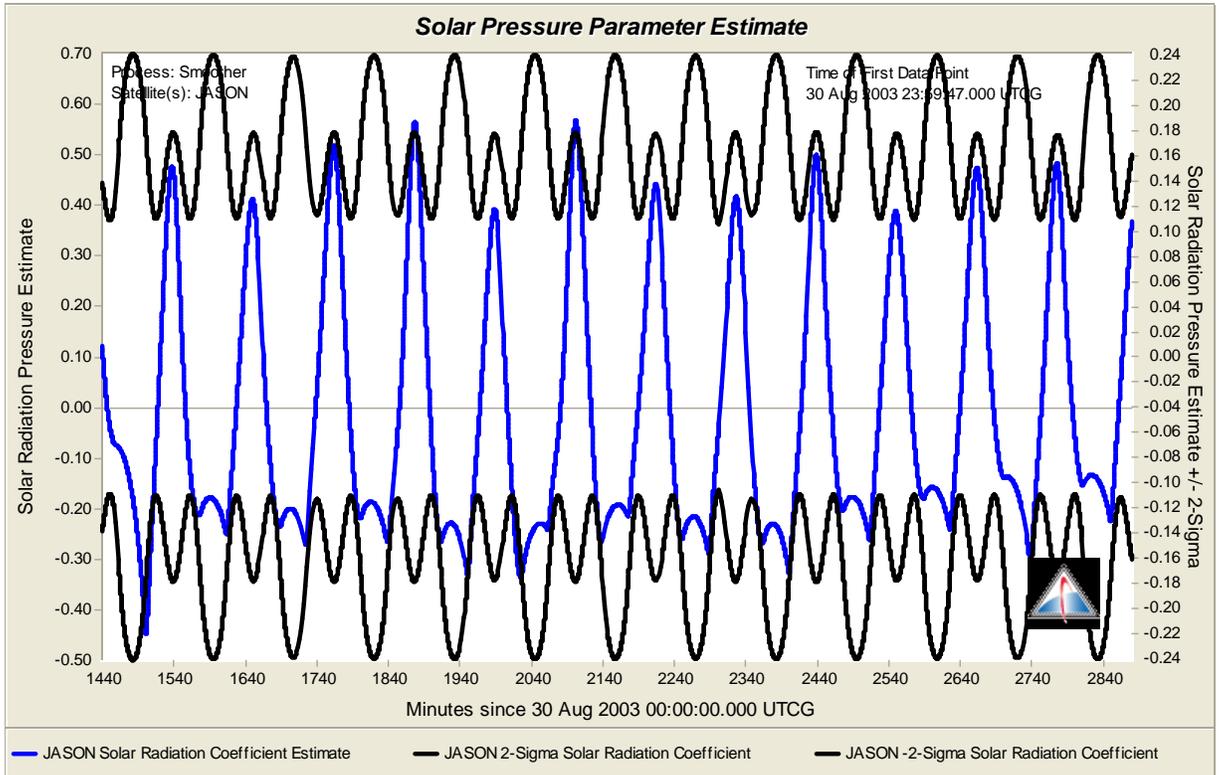Figure 17: JASON-GRACE Filter-Smoother Consistency Test 3

Figure 18: JASON Solar Pressure Error Smoother Estimate